

# 1 **Building Interface Bonding and Shield for Stable Li-rich Mn-based Oxide Cathode**

2  
3 Jun Chen<sup>a</sup>, Hongyi Chen<sup>a</sup>, Yu Mei<sup>a</sup>, Jinqiang Gao<sup>a</sup>, Alvin Dai<sup>b</sup>, Ye Tian<sup>a</sup>, Wentao Deng<sup>a</sup>,  
4 Guoqiang Zou<sup>a</sup>, Hongshuai Hou<sup>a</sup>, Craig E. Banks<sup>d</sup>, Tongchao Liu<sup>b\*</sup>, Khalil Amine<sup>b,c\*</sup>, Xiaobo  
5 Ji<sup>a\*</sup>

6  
7 <sup>a</sup> State Key Laboratory of Powder Metallurgy, College of Chemistry and Chemical Engineering,  
8 Central South University, Changsha, China

9 <sup>b</sup> Chemical Sciences and Engineering Division, Argonne National Laboratory, Lemont, IL,  
10 USA

11 <sup>c</sup> Material Science and Engineering, Stanford University, Stanford, CA, USA

12 <sup>d</sup> Division of Chemistry and Environmental Science, Manchester Metropolitan University,  
13 Manchester, M1 5GD, UK

14  
15 E-mail: liut@anl.gov; amine@anl.gov; xji@csu.edu.cn  
16  
17

18 **Abstract** Implementation of Li-rich Mn-based oxide cathode with high-energy-density has  
19 been restrained by capacity/voltage degradation that results from irreversible lattice oxygen loss  
20 and structure rearrangements. To resolve these challenges, in this work,  
21  $\text{Li}_{1.2}\text{Mn}_{0.54}\text{Ni}_{0.13}\text{Co}_{0.13}\text{O}_2$  encapsulated by amorphous  $\text{Co}_x\text{B}$  (CB-LRM) is rationally designed  
22 *via* autocatalytic plating for highly reversible cationic/anionic hybrid cathode material. Band  
23 coherency is ingeniously evoked by interface-reconstruction between bulk structure and  
24 amorphous coating layer, which lower the energy of O  $2p$  states. This is associated with  
25 strengthened orbital hybridization of O  $2p$ -Mn  $3d$  and increased formation energy of oxygen  
26 vacancy, which mitigates the lattice oxygen loss considerably. Additionally, interface shielding  
27 effects that protect electrode against electrolyte corrosion and the reduction of surface oxygen  
28 are also present with fully coverage of amorphous  $\text{Co}_x\text{B}$  coating layer. As a result, the as-  
29 designed CB-LRM cathode exhibits excellent cycle stability after 100 loops with only 0.154%  
30 per cycle capacity fade and improved voltage degradation. Given this, this work provides a  
31 potential avenue for rational design of lattice oxygen-based electrode materials with high-  
32 energy-density.

1 **Keywords:** Band coherency, interface shielding, autocatalytic plating, lattice oxygen redox, Li-  
2 rich Mn-based oxide cathode

### 4 **1. Introduction**

5 Li-rich Mn-based oxide (LRM) cathodes have attracted intensive attention as they render  
6 remarkable capacities by invoking redox chemistry on both transition metal (TM) and lattice  
7 oxygen.[1-3] However, owing to the intrinsic instability of oxygen anion, LRM cathode usually  
8 suffers from irreversible lattice oxygen loss.[4] It is widely accepted that, lattice oxygen loss  
9 accompanies side reaction at the LRM electrode/electrolyte interface that trigger the  
10 microscopic/macroscale structure evolutions, including the unidirectional phase  
11 transformation, the formation of thicker cathode electrolyte interface as well as  
12 structure/morphology fracture, ultimately leading to a fast capacity/voltage degradation.[3, 5]  
13 Therefore, enabling sustainable lattice oxygen redox and strengthening the electrode/electrolyte  
14 interface would be the key to boost the capability of Li<sup>+</sup> storage for LRM cathode materials.

15 Admittedly, much effort has been devoted to mitigating the fast electrochemical  
16 degradation, including constructing coating layer on the surface, engineering dopants into  
17 structure framework, and developing nano/micro-heterostructures. In particular, surface  
18 protective coating, a widely industrialized technology, has been effective at suppressing the  
19 parasitic reactions between surface lattice oxygen and electrolyte.[6-9] However, so far physical  
20 surface protection shows a negligible improvement in lattice oxygen reversibility, as  
21 demonstrated by the persistence of oxygen release and voltage fade when operating at high  
22 voltages. Once oxygen loss occurs on the surface, the energy barrier for TM migration will be  
23 greatly reduced, and irreversible phase transition will occur.[4] More importantly, the  
24 generation of surface oxygen vacancies will significantly accelerate the diffusion of bulk  
25 oxygen during extended cycling.[10] This phenomenon, together with the continuous  
26 irreversible phase transition, will activate lower-voltage redox chemistry, which has been  
27 considered as the governing cause of the capacity/voltage fading. Consequently, it is of  
28 particular importance to searching for a novel strategy that could simultaneously protect surface  
29 lattice oxygen from side reaction and enhance oxygen redox reversibility.

30 In this work, we designed a novel surface engineering LRM coupled with the band  
31 coherency and interface shielding effect, which dramatically improves the electrochemical  
32 performance of LRM cathode materials. Benefitting from an autocatalytic plating reaction, the  
33 LRM cathode materials are able to be fully encapsulated by amorphous Co<sub>x</sub>B. Interestingly,  
34 based on the unique physicochemical properties of Co<sub>x</sub>B,[11] we found that band coherency is

1 ingeniously excited by the interface bonding between surface structure of LRM and amorphous  
2  $\text{Co}_x\text{B}$  coating layer, which would lower the energy of O  $2p$  states associated with the  
3 strengthened orbital hybridization of O  $2p$ -Mn  $3d$  to elevate the formation energy of oxygen  
4 vacancy, thereby considerably mitigating the lattice oxygen loss. Simultaneously, interface  
5 shielding effect is invoked by the functionalized coating layer, which is beneficial for mitigating  
6 the side reaction along with subsequent TMs dissolution, and ultimately rendering a well-knit  
7 electrode/electrolyte interface. Expectedly, with the assistance of structure/interface coupling  
8 effect, the as-designed CB-LRM cathode renders excellent long cycling stability after 200 loops  
9 with only 0.1535% capacity fading and 3.35 mV voltage decline per cycle.

## 11 2. Result and Discussion

### 12 2.1 Dissecting the band coherency effect induced by the coating layer *via* density 13 functional theory calculation

14 Symmetry labels for  $\text{LiTMO}_2$  correspond to the conventional  $O_h$  point group of  $\text{TMO}_6$   
15 coordination, while those for  $\text{Li}_2\text{MnO}_3$  correspond to the  $C_{2v}$  point group of  $\text{OMn}_2\text{Li}_4$   
16 coordination.[9] In terms of Li-rich Mn-based oxide cathode, when O is coordinated by two  
17 Mn and four Li such as in  $\text{Li}_2\text{MnO}_3$  (Fig. 1c),[12, 13] the point symmetry of the  $\text{OMn}_2\text{Li}_4$   
18 octahedron is  $C_{2v}$ . According to the point symmetry, the molecular orbitals can be named as  
19 follows: four O  $2p$  orbitals constitute  $\sigma$ -type bonding ( $a_1$  and  $b_2$ ) and antibonding ( $a_1^*$  and  $b_2^*$ )  
20 molecular orbitals with Mn  $nd(e_g)$ ,  $(n+1)s$ , and  $(n+1)p$ , while two O  $2p$  orbitals along an Li-O-  
21 Li axis and two Mn  $nd(t_{2g})$  form  $\pi$ -type less-bonding ( $b_1$ ) and less-antibonding ( $b_1^*$ ) molecular  
22 orbitals (Fig. 1c-e). As previously reported,[4] in  $\text{Li}_2\text{MnO}_3$  cathode, the energy level of O  $2p$  is  
23 higher than that of the occupied Mn  $nd(t_{2g})$ . Thus, the occupied molecular orbital of  $b_1^*$  is primarily  
24 consisted of O  $2p$ , which is responsible for an additional lattice oxygen redox reaction (Fig. 1c-  
25 e). Importantly, before the lattice oxygen is oxidized, this  $\pi$ -type interaction between the  
26 occupied O  $2p$  and Mn  $nd(t_{2g})$  is weak (almost nonbonding), and the O  $2p$  orbital near the Fermi  
27 level appears to be “orphaned”. However, after the oxidation of this antibonding  $b_1^*$  molecular  
28 orbital occurs, the corresponding Mn-O bond would become more robust with the larger  $b_1/b_1^*$   
29 splitting (Fig. 1d, e), therefore stabilizing the oxidized oxygen anion. In short, in Li-rich Mn-  
30 based oxide cathode, the lattice oxygen redox could be modulated by designing the band  
31 features, based on the energetics in the crystal field theory. To demonstrate the feasibility of  
32 band coherency between bulk structure and coating layer for mitigating the lattice oxygen loss,  
33 density functional theory (DFT) calculations are firstly introduced. As shown in Fig. 1a, for the  
34 atomistic details, first-principles calculations are conducted on the (131) crystallographic plane

1 of  $\text{Li}_2\text{MnO}_3$  as well as on the interface between the  $\text{Li}_2\text{MnO}_3$  (131) crystallographic plane and  
2 amorphous  $\text{Co}_x\text{B}$ . It should be noticed that, as shown in Fig. 1b, at the interface between  
3  $\text{Li}_2\text{MnO}_3$  (131) crystallographic plane and amorphous  $\text{Co}_x\text{B}$ , Co and B are preferentially  
4 bonded with the surface lattice O of  $\text{Li}_2\text{MnO}_3$  (named as interface bonding effect), rather than  
5 with Li or Mn. The interfacial Co-O and B-O bonding are stronger than the lattice Mn-O  
6 bonding, as obviously indicated by the stronger electron cloud sharing for the former in the  
7 charge density plot (Fig. 1b). That is to say, the band coherency could be excited by the interface  
8 bonding effect to some extent, mainly resulted from the as-designed coating layer of amorphous  
9  $\text{Co}_x\text{B}$ . More importantly, the band coherency induced by the introduction of amorphous  $\text{Co}_x\text{B}$   
10 is beneficial for lowering the energy of O  $2p$  states (Fig. 1c-e), which have less high-energy  
11 states close to Fermi level than that of LRM (Fig. 1c). Therefore, it is concluded that, a band  
12 coherency triggered by the interface bonding effect is effectively manipulated by the formation  
13 of the bonding/antibonding  $b_1/b_1^*$  molecular orbitals through a  $\pi$ -type O  $2p$ -Mn  $3d(t_{2g})$   
14 interaction induced by the design of coating layer of amorphous  $\text{Co}_x\text{B}$ , and the corresponding  
15 Mn-O bond should become more vigorous with larger  $b_1/b_1^*$  splitting, thus enhancing the  
16 formation energy of oxygen vacancy and stabilizing the oxidized lattice oxygen (Fig. 1f).  
17 Therefore, it is expected that the band coherency induced by the design of functionalized  
18 coating layer of amorphous  $\text{Co}_x\text{B}$  is beneficial to enhance the stability of crystal structure and  
19 drive the reversible lattice oxygen redox, bring about the improved  $\text{Li}^+$  storage capacities.

20

## 21 **2.2 Demystifying the structure/morphology evolution triggered by the autocatalytic** 22 **plating**

23 By virtue of the insights from DFT calculations results above (Fig. 1). To adequately verify  
24 and take advantage of the mentioned physical properties for the functionalized coating layer.  
25 Pristine LRM, a typical polycrystalline microstructure with spherical secondary particles (Fig.  
26 2b, c), is prepared by a conventional co-precipitation route, followed by calcination with lithium  
27 hydroxide.[14] As expected, by using the autocatalytic plating strategy (Fig. 2a),[15, 16] the  
28 modified LRM (denoted as CB-LRM) with integrally encapsulated by amorphous  $\text{Co}_x\text{B}$  is  
29 successfully designed (Fig. 2e, f and Fig. 4a, g), and the detailed method is displayed in  
30 Supporting Information. Accordingly, the atomic compositions of the as-prepared samples are  
31 listed based on the results of inductive coupled plasma emission spectrometer (ICP), as  
32 presented in Table S1 with normalized formula  $\text{Li}_{1.2}\text{Mn}_{0.54}\text{Ni}_{0.13}\text{Co}_{0.13}\text{O}_2$  for the pristine LRM.  
33 Note that the compositions of amorphous  $\text{Co}_x\text{B}$  are close to  $\text{Co}_{2.3}\text{B}$ . Furthermore, their crystal  
34 structures are investigated by X-ray diffraction (XRD), as shown in Fig. 3a, b, all diffraction

1 peaks are accurately labeled with a hexagonal  $\alpha$ -NaFeO<sub>2</sub> (space group:  $R-3m$ ), except for  
2 weaker superlattice diffraction characteristic peaks between 20° and 23°, which are attributed  
3 to the (020) and (110) diffraction peaks of monoclinic Li<sub>2</sub>MnO<sub>3</sub> (space group:  $C2/m$ ), mainly  
4 resulted from the unique Li/Mn local ordering in the TM layers.[17] Moreover, it is found that,  
5 no characteristic diffraction peaks of Co<sub>x</sub>B are observed in Fig. S1a, demonstrating that the as-  
6 obtained Co<sub>x</sub>B coating layers are presented as amorphous feature. It should be emphasized that  
7 the distinct splitting-diffraction peaks of (006)/(012) and (018)/(110) are obviously presented  
8 (Fig. S1c), thoroughly showing that both LRM and CB-LRM have a well ordered layered  
9 structure, that is to say, which is beneficial to improve the Li<sup>+</sup> shuttling.[18] These results above  
10 are in good line with those of previous studies,[12] and STEM with annular bright-field (ABF)  
11 as well as high angle annular dark-field (HAADF) images (Fig. 4d-f). Moreover, it is  
12 noteworthy that, in clear, the intensity of (003) diffraction peak for the pristine LRM is stronger  
13 than that of CB-LRM (Fig. S1b), which is perhaps ascribed that the exposure of the bulk  
14 materials is partly shielded by the coating layer of amorphous Co<sub>x</sub>B,[14] unambiguously  
15 suggesting that the coating layer has been successfully adhered on the surface of LRM.  
16 Resultantly, the coating layer of amorphous Co<sub>x</sub>B, as confirmed above, may be good for  
17 mitigating the side reaction of electrode/electrolyte interface and stabilizing the lattice oxygen,  
18 thereby enhancing the reversibility of Li<sup>+</sup> storage.

19 Multiscale characterizations are further employed to investigate the structure properties of  
20 Co<sub>x</sub>B surface coating. As shown in Fig. 2b-g, the coating layers of amorphous Co<sub>x</sub>B (~ 20 nm)  
21 with hierarchical structure are confirmed by the high-resolution field emission scanning  
22 electron microscope (FE-SEM) (Fig. 2e, f) and STEM (Fig. 4a). The mapping images of  
23 electron energy loss spectroscopy (EELS) also reveal that the bulk structure of CB-LRM is  
24 integrally covered by amorphous Co<sub>x</sub>B (Fig. 4g, h), which may be beneficial for evoking the  
25 band coherency between the bulk structure and coating layer through the interface bonding  
26 effect as well as protecting the active materials,[19, 20] to some extent. To gain better  
27 understanding of the interface bonding effect, X-ray photoelectron spectroscopy (XPS) analysis  
28 is applied to further explore the surface state and interfacial interaction of the as-designed  
29 samples. As shown in Fig. 3d-f, the CB-LRM with completely covered by amorphous Co<sub>x</sub>B is  
30 also confirmed by the intrigued evolution of XPS spectra, as expected. Interestingly, the distinct  
31 B-O bonding is clearly observed for CB-LRM (Fig. 3d, f), regarded as interface bonding effect,  
32 which would be conducive to exciting the band coherency as well as stabilizing the lattice  
33 oxygen and reinforcing the stability of crystal structure through the interface bonding effect.  
34 These intriguing phenomena are in good line with DFT results (Fig. 1). Based on the results

1 above, it is proposed that, the structure/interface coupling effect would be evoked by the coating  
2 layer of amorphous  $\text{Co}_x\text{B}$ , which would be levers to strengthen the lattice oxygen and protect  
3 the active materials, therefore improving the capability of  $\text{Li}^+$  storage.

4 The fine structures of CB-LRM at the atomic scale are systematically probed by  
5 ABF/HAADF-STEM. As shown in Fig. 4d, e, the positions of TMs atoms are presented by  
6 bright-dot in HAADF-STEM images and dark-dot in ABF-STEM images. Both ABF and  
7 HAADF images confirm a typical composite structure composing of  $R-3m$  and  $C2/m$  space  
8 group, which is well consistent with the XRD results.[9, 21] Moreover, the amorphous structure  
9 of  $\text{Co}_x\text{B}$  coating layer is further confirmed by atomic resolution HAADF-STEM (Fig. 4g). The  
10 uniformity of  $\text{Co}_x\text{B}$  coating is conducive to building band coherency between the bulk structure  
11 and coating layer as well as surface shielding effects, thus stabilizing the lattice oxygen and  
12 mitigating the side reaction of electrode/electrolyte interface to elevate the capability of  $\text{Li}^+$   
13 storage.

### 15 **2.3. Conveying the $\text{Li}^+$ storage features invoked by structure/interface coupling effect**

16 Since the uniform  $\text{Co}_x\text{B}$  coating has been successfully built up, it is of particular interest  
17 to investigate its electrochemical properties. The coin-type cells are assembled utilizing the as-  
18 designed materials as a cathode to evaluate their  $\text{Li}^+$  storage features within a voltage range of  
19 2.0-4.8 V. As shown in Fig. 5a, the initial discharge capacities of the LRM as well as CB-LRM  
20 are calculated to be 281.92 and 310.4  $\text{mAh g}^{-1}$ , and its Coulombic efficiency (CE) are recorded  
21 as 81.8% and 88.0%, respectively, demonstrating that the surface side reaction is considerably  
22 mitigated by the structure/interface coupling effect evoked by the coating layer of amorphous  
23  $\text{Co}_x\text{B}$ . Moreover, surface oxygen evolution is further studied by *in situ* differential  
24 electrochemical mass spectrometry (Fig. 5b, c) and cyclic voltammetry (CV) (Fig. 5d, g) results.  
25 Clearly, oxygen release in the form of  $\text{CO}_2$  has been effectively mitigated by amorphous  $\text{Co}_x\text{B}$   
26 coating, benefitting from the interface bonding and shield effects. Note that the reduced energy  
27 barrier for the charge transfer (Fig. 5f, i) and the strengthened electrode/electrolyte interface  
28 eventually can facilitate the interfacial transportation process and improve rate capabilities (Fig.  
29 S5). Accordingly, the kinetic of  $\text{Li}^+$  diffusion for the as-designed materials is systematically  
30 studied through galvanostatic intermittent titration technique (GITT). As shown in Fig. S6a-f,  
31 one selected region at the charging process ( $\sim 4.4$  V) is utilized to evaluate the polarization  
32 electrochemical process and diffusion capability of  $\text{Li}^+$ . The smaller  $\Delta E_t$  and  $iR$  are clearly  
33 presented, suggesting that the  $\text{Li}^+$  diffusion for CB-LRM is efficiently improved, in great line  
34 with the electrochemical impedance spectroscopy (EIS) and CV results (Fig. S7 and Fig. 5e, h).

1 Furthermore, to further evaluate their practical application in LIBs, cycling performance of the  
2 as-designed materials at different current densities are collected to study the effect of coating  
3 layer of amorphous  $\text{Co}_x\text{B}$  (Fig. 5j-1 and Fig. S8). As expected, the discharging specific capacity  
4 of CB-LRM could be retained at  $218.9 \text{ mAh g}^{-1}$  after 100 loops at 2 C, much higher than that  
5 of LRM ( $189.7 \text{ mAh g}^{-1}$ ) (Fig. 5l). It is anticipated that, as presented in Fig. 5j, the average  
6 voltage decay of discharge process for CB-LRM is only 0.26 V (2.6 mV per cycle) after 100  
7 loops at 1 C. By contrast, the average attenuation of discharging potential for LRM is about  
8 0.317 V (3.17 mV per cycle). Owing to the slower capacity declining and lower voltage  
9 degradation (Fig. S9), more than 78.92% energy retention can be retained after 100 cycles for  
10 CB-LRM, in contrast, a low energy retention of 72.11% is presented for LRM (Fig. S8b). Such  
11 an outstanding cycling stability for CB-LRM should be ascribed to the mitigated lattice oxygen  
12 loss, improved stabilities of crystal structure and electrode/electrolyte interface. Based on the  
13 discussion above, it is summarized that the superior capabilities of  $\text{Li}^+$  storage for CB-LRM are  
14 successfully realized. Evidently, the excellent electrochemical properties are closely related to  
15 the structure/interface coupling effect invoked by the coating layer of amorphous  $\text{Co}_x\text{B}$ .

16

#### 17 **2.4. Unscrambling the electrode/electrolyte interface evolution**

18 As confirmed by the electrochemical performances above, the structure/interface coupling  
19 effect induced by the coating layer of amorphous  $\text{Co}_x\text{B}$  is conducive to driving the reversible  
20 lattice oxygen redox, rendering the improved reversibility of  $\text{Li}^+$  storage. It is well known that,  
21 the electrode/electrolyte interface traits are also paramount to the electrochemical  
22 performances.[22] It is well documented that intergranular cracking between connected primary  
23 particles in a secondary sphere is a critical issue for the degradation of cathodes, especially with  
24 higher cut-off voltages and prolonged cycling, mainly leading to the loss of electrical contacts  
25 between primary particles, blocking the charge carrier transportation, and finally deteriorating  
26 the capability of  $\text{Li}^+$  storage[23, 24]. Moreover, the intergranular cracking is mostly related to  
27 mechanical stress produced by anisotropic lattice expansion/shrinkage and heterogeneous  
28 charge/discharge kinetics during the electrochemical cycle. To further verify the advantages of  
29 structure/interface coupling effect and systematically probe the electrode/electrolyte interface  
30 traits, FE-SEM images of the cycled electrodes are utilized to observe morphology intergraty  
31 of as prepared CB-LRM and LRM cathodes. As shown in Fig. 6a, b, the broken secondary  
32 spheres are obviously observed in LRM electrode due to the anisotropic volume changes  
33 associated with the irreversible structure rearrangements and intergranular stress corrosion  
34 cracking, which should mainly account for the capacity/voltage decline. In addition, numerous

1 microcracks distributed over the microsphere are found for the LRM electrode after the  
2 prolonged cycling, which are usually generated along the grain boundaries from the core and  
3 propagated to the surface resulted from the inner anisotropic strain and HF corrosion (Fig. 6a,  
4 b). These microcracks undermine the mechanical integrity of the cathode and induce the  
5 electrolyte penetration into the particle core, which would exacerbate the surface degradation  
6 of the internal primary particles. In contrast, well-preserved rectangular-like morphology and  
7 mechanically intact without clear cracks are presented for CB-LRM electrode (Fig. 6d, e),  
8 owing to the advantages of structure/interface coupling effect aroused by the coating layer of  
9 amorphous  $\text{Co}_x\text{B}$ . Furthermore, the HAADF-STEM images of the cycled electrode (Fig. S10)  
10 demonstrated that the full encapsulation with the activated interface bonding and shield effect  
11 is conducive to mitigating the irreversible phase transformation, therefore enhancing the  
12 stability of crystal structure and boosting the  $\text{Li}^+$  storage capability. Note that, complete  
13 elimination of the cracking is still challenging if ever possible, nevertheless, a satisfactory  
14 cycling performances over hundreds of cycles may be achieved. The potential mechanism of  
15 the robust electrode/electrolyte interface induced by the introduction of coating layer would be  
16 further discussed as follow, in details.

17       It should be pointed out that, the decomposition of electrolyte is considerably aggravated  
18 when oxygen radicals are formed in the electrolyte (*e.g.*, hydroxyl  $\text{HO}^\bullet$ , superoxide  $\text{O}^{2\bullet}$  or  $\text{O}_2$ ),  
19 which could oxidize the carbonate-solvent under high voltage.[22, 25, 26] As expected, the  
20 curbed oxygen-radicals from the CB-LRM cathode in the electrolyte would greatly mitigate the  
21 cathode electrolyte interface over-growth. To further explore the evolution of  
22 electrode/electrolyte interface induced by the coating layer of amorphous  $\text{Co}_x\text{B}$ , XPS is firstly  
23 employed to examine the chemical bonding environment of the cathode surface, with the  
24 spectra from C  $1s$ , B  $1s$ , Co  $2p$  and Mn  $2p$  shown in Fig. S11, in which the signals of C  $1s$   
25 (contributed by organic cathode electrolyte interface components, such as polycarbonates and  
26 semicarbonates), Co/Mn  $2p$  signals (contributed by Co/Mn-containing cathode electrolyte  
27 interface components, such as Co/MnF<sub>2</sub>) are observed in cycled pristine LRM and CB-LRM.  
28 And, it is found that the intensities of XPS spectra for LRM are stronger than that of CB-LRM.  
29 Meanwhile, strong Co  $2p$  and B  $1s$  signals are observed in cycled CB-LRM (Fig. S11a, d),  
30 indicating that the coating layer of  $\text{Co}_x\text{B}$  is not fully covered by thick cathode electrolyte  
31 interface, even after the prolonged cycling. Furthermore, the electrode/electrolyte interface of  
32 the cycled electrode are also investigated by the TEM, as shown in Fig. S12, the thin cathode  
33 electrolyte interface of CB-LRM after 200 cycles at 2 C demonstrated that the amorphous  $\text{Co}_x\text{B}$   
34 coating is conducive to reducing the thickness of cathode electrolyte interface, which are mainly

1 resulted from the mitigated the lattice oxygen loss accompanied with the electrolyte  
2 decomposition. All the phenomena above suggest a suppressed cathode electrolyte interface  
3 over-growth in CB-LRM, mainly resulted from the structure/interface coupling effect induced  
4 by the coating layer of amorphous  $\text{Co}_x\text{B}$ . Moreover, it should be awared that, the limited  
5 probing depth of X-rays used in XPS only captures the chemical bonding environment on the  
6 surface and does not provide any information on the layer thickness. Note that, Time of flight  
7 secondary ion mass spectrometry (TOF-SIMS) is a powerful tool for investigating the chemical  
8 composition, layer thickness, and depth distribution of the decomposition species in the cathode  
9 electrolyte interface layer. Therefore, the TOF-SIMS is further applied to investigate the  
10 electrode surface after 200 loops at 2 C and conducted the three dimensions (3D) surface  
11 reconstruction. Clearly, LRM electrodes are dramatically collapsed as its surface became very  
12 rough with much cavity (Fig. 6g-j), in contrast, CB-LRM particles remained well integrated  
13 and smooth (Fig. 6k-n), in good line with SEM images in Fig. 6a-f, adequately demonstrating  
14 that the construction of coating layer of  $\text{Co}_x\text{B}$  is beneficial for enhancing the stability of crystal  
15 structure and electrode/electrolyte interface. Usually, the  $\text{C}_2\text{H}^-$  (Fig. S13b, h) and  $\text{C}_2\text{HO}^-$  (Fig.  
16 S13f, l) fragments are employed to denote the cathode electrolyte interface component in the  
17 3D reconstruction. It is worth noting that, much thinner cathode electrolyte interface layer  
18 adhering on the cycled CB-LRM cathode than on the cycled LRM electrode demonstrate that  
19 it obviously remained stable in the CB-LRM cycling, nevertheless, while the carbonate-solvent  
20 is seriously destroyed in the LRM cycling. In addition, the  $\text{PO}_2^-$  (Fig. S13d, j) and  $\text{PO}_3^-$  (Fig.  
21 S13e, k) are mainly related to the decomposition of electrolyte. Notably, a relatively weak of  
22  $\text{PO}_2^-$  (Fig. S13j) and  $\text{PO}_3^-$  (Fig. S13k) signals for the CB-LRM electrode is noticed indicating  
23 that the electrolyte decomposition at the CB-LRM cathode is considerably suppressed, in good  
24 line with the FE-SEM images (Fig. 6a-e). As shown in Fig. 7a-d and Fig. S13, 3D visualizations  
25 are well matched with the abovementioned spectral results (Fig. 7e, f). Moreover, CB-LRM  
26 cathode surface also prevented acidic corrosion from the side-products (*e.g.*, HF) in the  
27 electrolyte, as the  $\text{PF}_6^-$  (Fig. S13i), and  $\text{MnF}_3^-$  (Fig. S13g) layers at the CB-LRM cathode surface  
28 are much thinner than those at LRM cathode surface (Fig. S13a, c) after 200 loops. The lattice  
29 oxygen loss and dissolved TMs in the electrolyte are beneficial to facilitate the thermodynamic  
30 and kinetic advantage to the initiation and propagation of stress-corrosion cracking and degrade  
31 the cathodes. Evidently, TMs dissolution could be considerably suppressed by mitigating the  
32 electrolyte decomposition through the construction of coating layer of amorphous  $\text{Co}_x\text{B}$ .  
33 Furthermore, considerably uniform  $\text{LiF}_2^-$  in the CB-LRM is observed, indicating that the  
34 cathode electrolyte interface derived from the CB-LRM should be consisted of more LiF-like

1 inorganic components (which are known to be ‘well’ cathode electrolyte interface components).  
2 Note that the overall structure of the cathode electrolyte interface in both LRM and CB-LRM  
3 cathodes displays a double-layer (as indicated by the yellow and blue areas in Fig. 7e, f): the  
4 outer layer primarily consists of metal-related species ( $\text{LiF}_2$ ,  $\text{MnF}_3^-$ , etc.), while the inner layer  
5 is dominated by the electrolyte decomposition-bearing fragments. Besides, the cathode  
6 electrolyte interface species in LRM extend to a longer depth on the surface than in CB-LRM,  
7 implying the formation of a thicker cathode electrolyte interface on LRM after cycling. Taken  
8 together, much-thinner and robust cathode electrolyte interface layer at the CB-LRM cathode  
9 surface, presenting less fluoride, would be conducive to faster  $\text{Li}^+$  transfer, mitigating the TMs  
10 dissolution and safeguarding the TMs redox couples, verified by the EIS (Fig. S7) and GITT  
11 results (Fig. S6). In brief, these intrigued phenomena considerably confirmed that the coating  
12 layer of amorphous  $\text{Co}_x\text{B}$  for the CB-LRM is conducive to dramatically mitigating the  
13 electrolyte decomposition and subsequent TMs dissolution, resulting in a ruggedized  
14 electrode/electrolyte interface and structure/thermal stability. Based on the results above, it is  
15 concluded that the construction of coating layer of amorphous  $\text{Co}_x\text{B}$  would arouse the  
16 structure/interface coupling effect, which are beneficial for driving the reversible lattice oxygen  
17 redox induced by the excited interface-reconstruction and boosting the stability of  
18 electrode/electrolyte interface resulted from the alleviated cauterization of electrolyte invoked  
19 by the electrolyte decomposition. Furthermore, it is proposed that engineering the  
20 functionalized coating layer with interface bonding effect would be a potential route to optimize  
21 the electrochemical performances of Li-rich Mn-based oxide cathodes or the congeneric  
22 electrode materials. The suggested structure/interface coupling effect and its mitigation offer  
23 new insights into the intertwined electro-chemo-mechanics of oxide cathodes under fickle  
24 electrochemical environments and consistent with recent advance in optimizing bulk electrode  
25 composition and crystallography.

26

### 27 **3. Conclusions**

28 In summary, CB-LRM with integrally encapsulated by amorphous  $\text{Co}_x\text{B}$  is successfully  
29 designed *via* an autocatalytic plating strategy. Interestingly, band coherency is ingeniously  
30 invoked by the interface-reconstruction between bulk structure and amorphous coating layer,  
31 which would lower the energy of O  $2p$  states associated with the strengthened orbital  
32 hybridization of O  $2p$ -Mn  $3d$  to increase the formation energy of oxygen vacancies, therefore  
33 considerably mitigating the lattice oxygen loss. Meanwhile, interface shielding effect is aroused  
34 by the integrally coating layer of amorphous  $\text{Co}_x\text{B}$ , which is conducive to protecting the

1 electrode against the electrolyte corrosion along with subsequent TMs dissolution, and  
2 ultimately rendering a well-knit electrode/electrolyte interface. Greatly, the as-designed CB-  
3 LRM renders excellent long cycling stability after 100 loops with only 0.154% capacity fading  
4 and 2.60 mV potential decline per cycle. Meaningfully, such strategy is anticipated to offer  
5 reference for rationally designing the congeneric energy-storage materials.

#### 6 7 **Data availability**

8 The raw/processed data can be provided by authors upon reasonable request.

#### 9 10 **Authorship contribution**

11 **Jun Chen:** Conceptualization, Methodology, Investigation, Data curation, Writing – original  
12 draft, Writing – review & editing. **Hongyi Chen:** Visualization, Data curation, Writing – review  
13 & editing. **Xiaobo Ji:** Conceptualization, Methodology, Investigation, Writing – review &  
14 editing, Supervision. **Yu Mei:** Writing – review & editing. **Jinqiang Gao:** Writing – review &  
15 editing. **Alvin Dai:** Writing – review & editing. **Ye Tian:** Writing –review & editing. **Wentao**  
16 **Deng:** Writing – review & editing. **Guoqiang Zou:** Writing – review & editing. **Hongshuai**  
17 **Hou:** Writing – review & editing. **Craig E. Banks:** Writing – review & editing. **Xiaobo Ji:**  
18 Supervision. **Tongchao Liu:** Supervision. **Khalil Amine:** Supervision.

#### 19 20 **Declaration of Competing Interest**

21 The authors declare that they have no known competing financial interests or personal  
22 relationships that could have appeared to influence the work reported in this paper.

#### 23 24 **Acknowledgements**

25 This work was financially supported by National Natural Science Foundation of China  
26 (U20A20247), National Key Research and Development Program of China  
27 (2019YFC1907805) and Fundamental Research Funds for the Central Universities of Central  
28 South University (2021zzts0072). A.D, T.L and K.A acknowledge support from the US  
29 Department of Energy (DOE), Office of Energy Efficiency and Renewable Energy (EERE),  
30 Vehicle Technologies Office (VTO). This work was also supported by Clean Vehicles, US-  
31 China Clean Energy Research Centre (CERC-CVC2) under the US DOE EERE Vehicle  
32 Technologies Office. This research used resources of the Center for Nanoscale Materials  
33 including transmission electron microscopy, U.S. Department of Energy (DOE) Office of  
34 Science User Facilities operated for the DOE Office of Science and Office of Basic Energy

1 Sciences. Argonne National Laboratory is operated for the DOE Office of Science by the  
2 UChicago Argonne, LLC, under contract no. DE-AC02-06CH11357. J.C. thanks the Shiyanjia  
3 Lab ([www.shiyanjia.com](http://www.shiyanjia.com)) for the STEM and XPS characterization as well as Chunlin Tan  
4 (Wechat: EditorTan) for his help with the image illustrations.

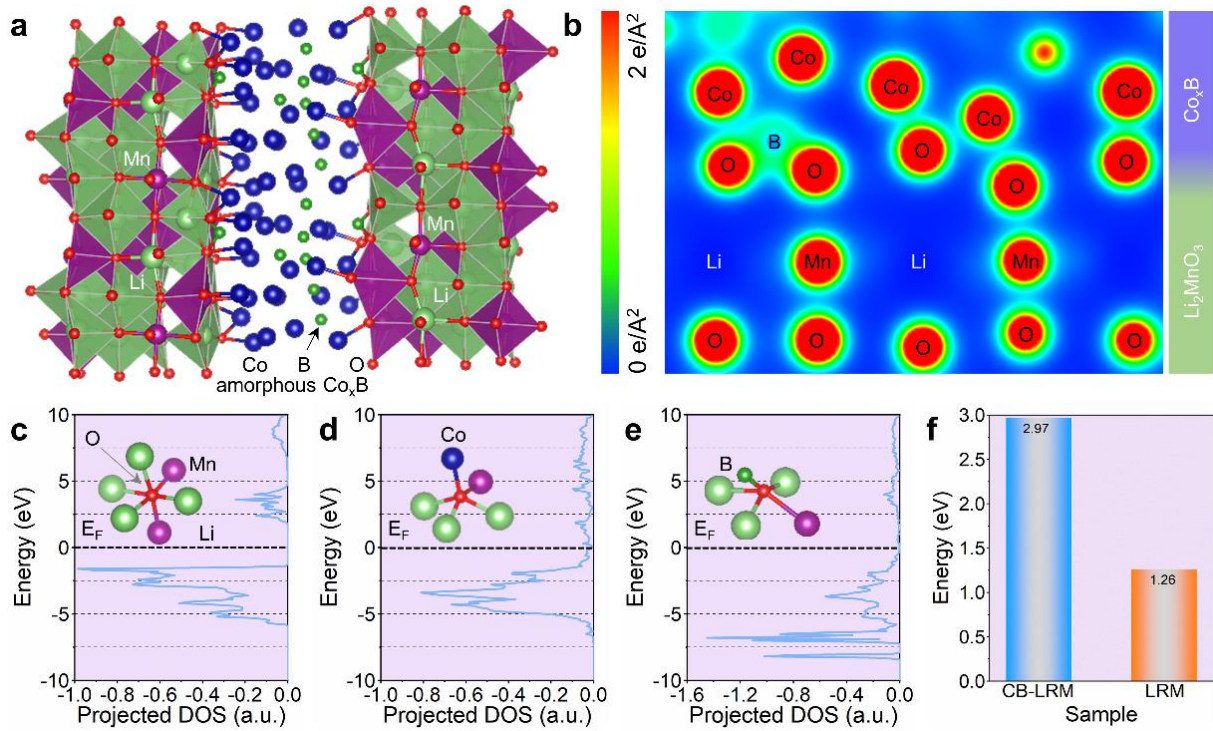


**Fig. 1.** Density functional theory calculation of the globally band coherency. (a) Atomic structure of the coating engineering. (b) 2 dimensional slices of the charge density distribution of a simulated interface between the  $\text{Li}_2\text{MnO}_3$  (131) surface and amorphous  $\text{Co}_x\text{B}$ . Projected density of states and schematic local environment (c-e insets) of lattice oxygen coordinated by two Mn and four Li atoms (c), interface oxygen coordinated by one Co, one Mn and three Li atoms (d) and interface oxygen coordinated by one B, one Mn and three Li atoms (e). (f) Formation energy of oxygen vacancy.

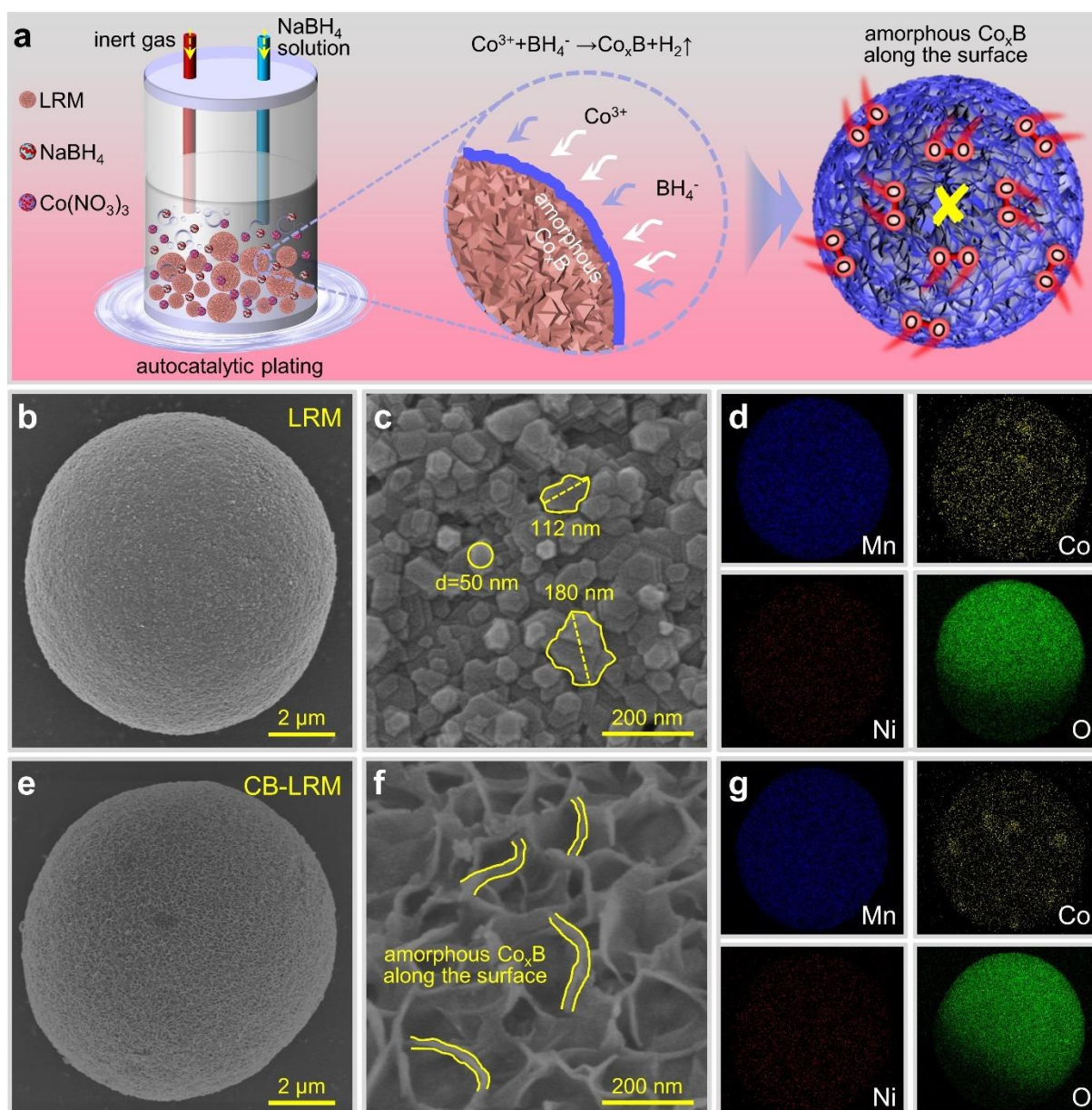


**Fig. 2.** Schematic illustration of the autocatalytic plating and morphology characterization for the as-designed samples. (a) Schematic illustration of the preparation process of the CB-LRM. The morphology characterization and EDS mapping images for the as-prepared (b-d) pristine LRM and (e-g) CB-LRM, respectively.

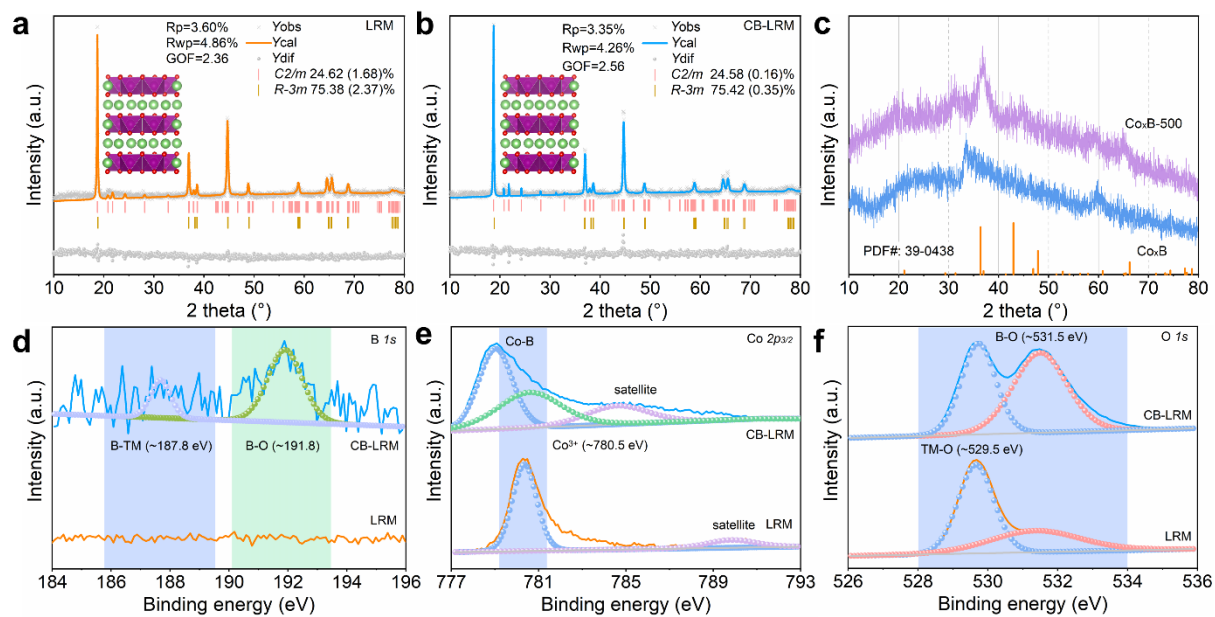


**Fig. 3.** Demystifying the crystal structure and surface composition of the as-obtained samples. (a, b) Rietveld refinements results of XRD patterns for the as-obtained samples. (c) XRD patterns of the as-prepared  $\text{Co}_x\text{B}$ . (d-f) XPS spectra of B  $1s$ , Co  $2p$  and O  $1s$  for the as-designed samples.

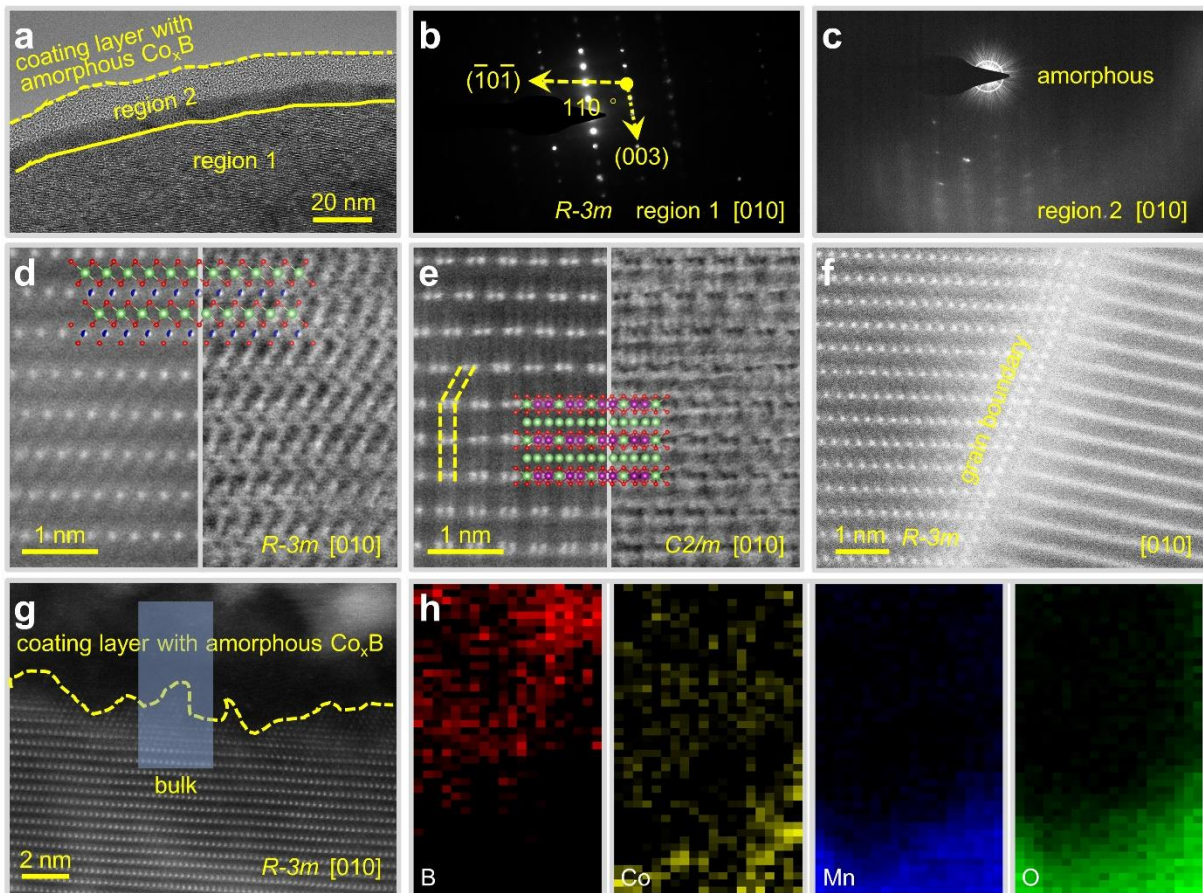


**Fig. 4.** Structure/interface characterization for the CB-LRM. (a-c) TEM and SAED images. (d-f) ABF/HAADF-STEM images. (g, h) HAADF-STEM and EELS mapping images.

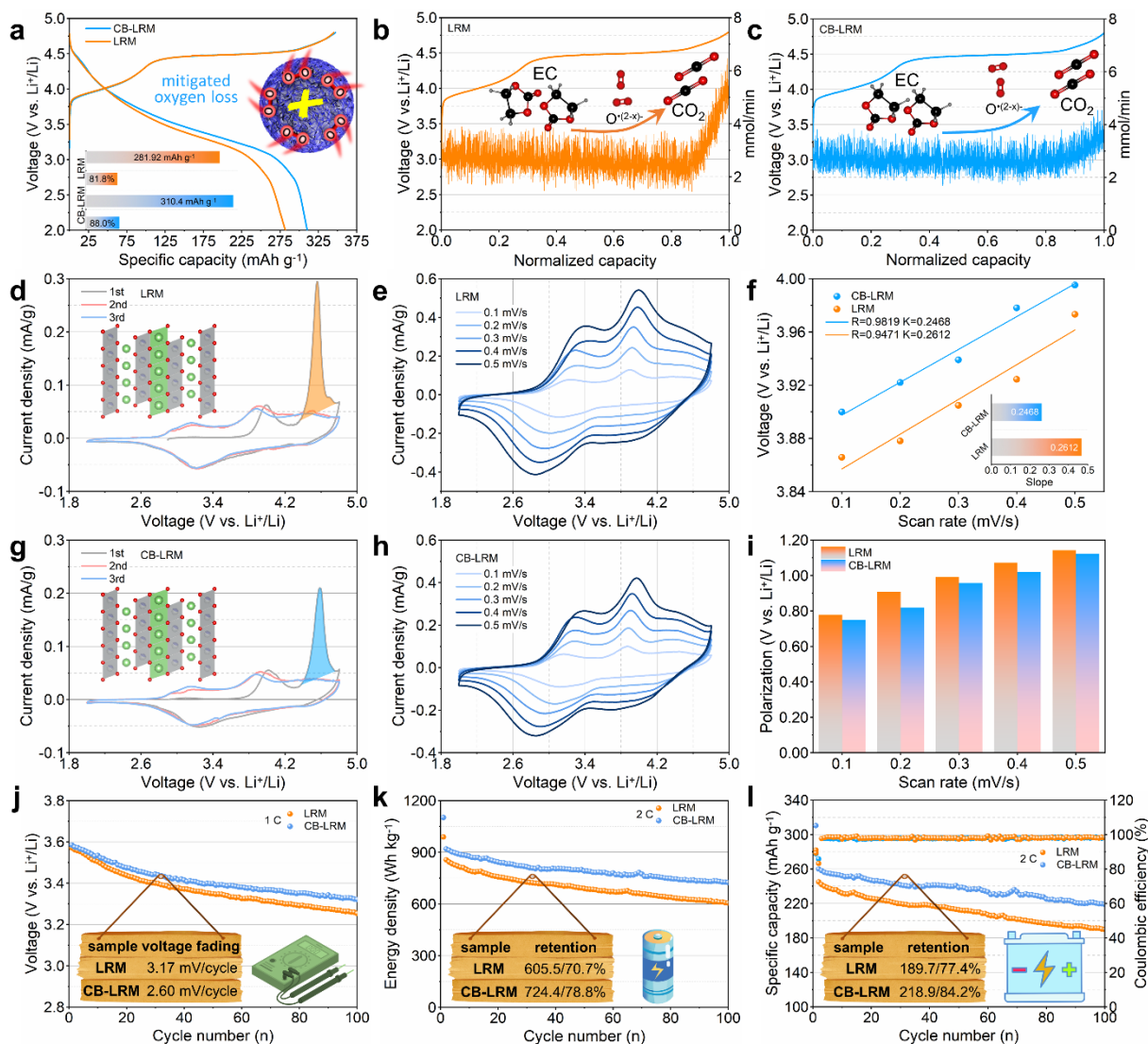


**Fig. 5.** Conveying the Li<sup>+</sup> storage features invoked by the structure/interface coupling effect. (a) Initial charge-discharge curves and the corresponding CE at 0.1 C. (b, c) CO<sub>2</sub> ( $m/z=44$ ) gas evolution and corresponding voltage profiles. (d, g) CV curves at 0.05 mV/s. (e, h). CV curves at different scan rate. (f, i) Voltage gap and polarization. (j) Average voltage of the as-obtained samples at 1 C. (k, l) Energy density and specific capacity of the as-obtained samples at 2 C, respectively.

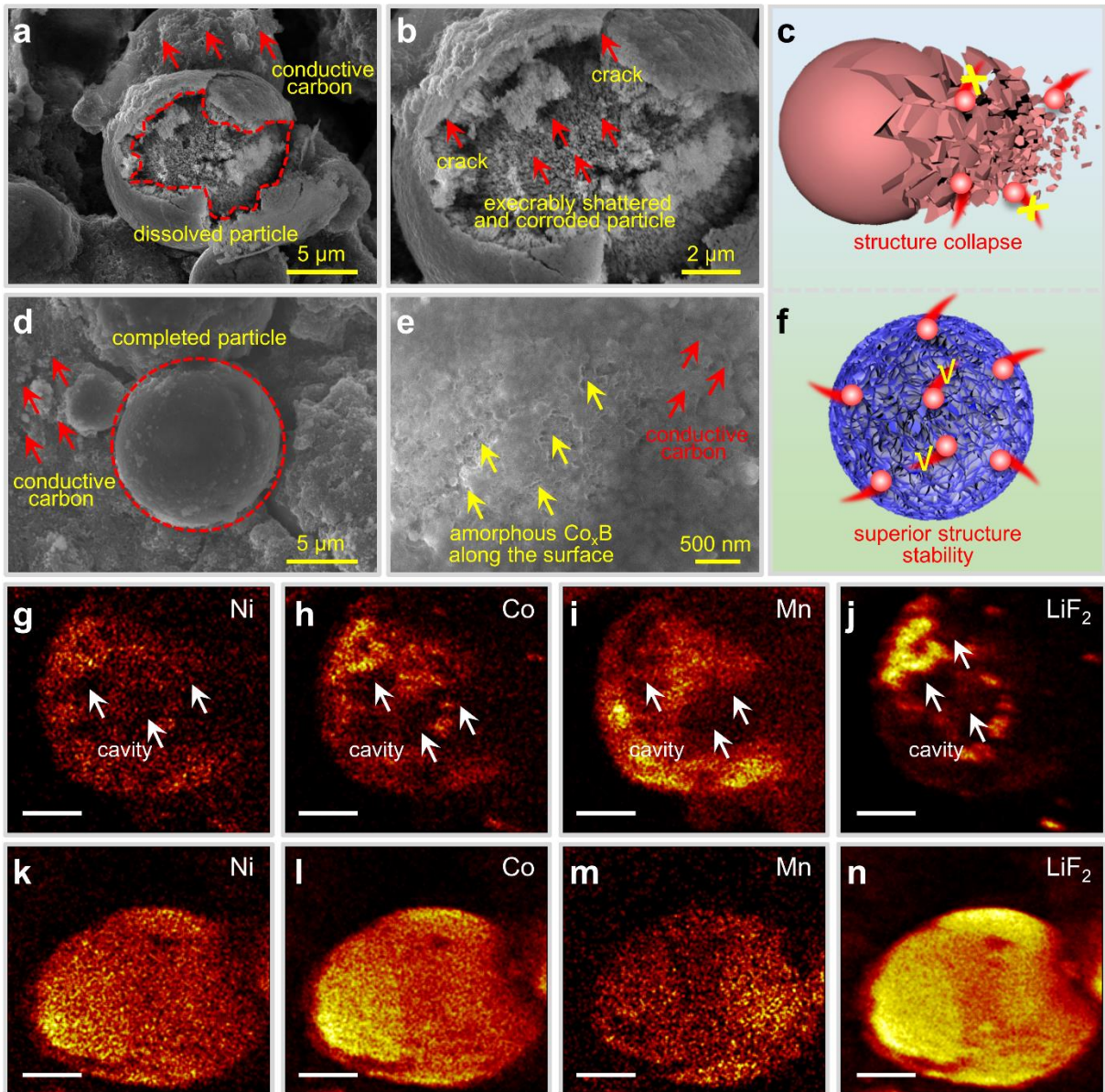


**Fig. 6.** Morphology and chemical composition evolution after 200 cycles at 2 C. Morphology transformation of (a-c) LRM and (d-f) CB-LRM electrodes. Comparative chemical mapping of various secondary-ion species as a function of sputtering time, demonstrating the complexity, and dynamic evolution of the cathode interphase of (g-j) LRM and (k-n) CB-LRM, respectively. Scale bars, 3  $\mu\text{m}$  (g-n).

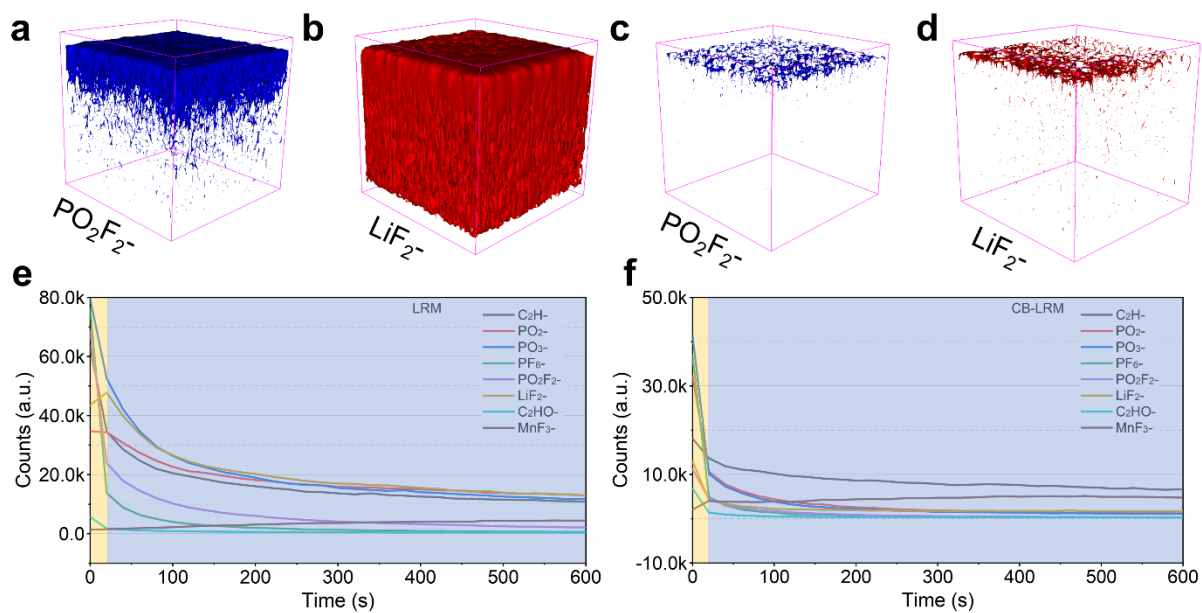


**Fig. 7.** Dissecting the electrode/electrolyte interface evolution after 200 cycles at 2 C. (a, b) The 3D reconstruction of  $\text{PO}_2\text{F}_2^-$  and  $\text{LiF}_2^-$  fragment for the LRM electrodes. (c, d) The 3D reconstruction of  $\text{PO}_2\text{F}_2^-$  and  $\text{LiF}_2^-$  fragment for the CB-LRM electrodes. (e, f) TOF-SIMS normalized depth profiles of diverse kinds of secondary-ion fragments constituting the cathode electrolyte interface of LRM and CB-LRM, respectively.

## References

- [1] J. Liu, J. Wang, Y. Ni, K. Zhang, F. Cheng, J. Chen, *Mater. Today*, 43 (2021) 132-165.
- [2] H. Hasnain, S. Kosuke, B. Bernardo, T. Naruki, Y. Naoaki, Y. Kentaro, O. Yuki, U. Yoshiharu, S. Yoshiharu, S. Hiroshi, B. Arun, V. Venkatasubramanian, *Nature*, 594 (2021) 213-216.
- [3] P.M. Csernica, S.S. Kalirai, W.E. Gent, K. Lim, Y.-S. Yu, Y. Liu, S.-J. Ahn, E. Kaeli, X. Xu, K.H. Stone, A.F. Marshall, R. Sinclair, D.A. Shapiro, M.F. Toney, W.C. Chueh, *Nat. Energy*, 6 (2021) 642–652.
- [4] R.A. House, J.-J. Marie, M.A. Pérez-Osorio, G.J. Rees, E. Boivin, P.G. Bruce, *Nat. Energy*, 6 (2021) 781-789.
- [5] S. Yin, W. Deng, J. Chen, X. Gao, G. Zou, H. Hou, X. Ji, *Nano Energy*, 83 (2021) 105854.
- [6] W. He, W. Guo, H. Wu, L. Lin, Q. Liu, X. Han, Q. Xie, P. Liu, H. Zheng, L. Wang, X. Yu, D.-L. Peng, *Adv. Mater.*, (2021) 2005937.
- [7] H. Hou, C.E. Banks, M. Jing, Y. Zhang, X. Ji, *Adv. Mater.*, 27 (2015) 7861-7866.
- [8] T. Liu, J. Liu, L. Li, L. Yu, J. Diao, T. Zhou, S. Li, A. Dai, W. Zhao, Xu, S. Y. Ren, L. Wang, T. Wu, R. Qi, Y. Xiao, J. Zheng, W. Cha, R. Harder, I. Robinson, J. Wen, J. Lu, F. Pan, K. Amine, Origin of structural degradation in Li-rich layered oxide cathode. *Nature*, (2022) 606, 305-312.
- [9] T. Liu, L. Yu, J. Liu, J. Lu, X. Bi, A. Dai, M. Li, M. Li, Z. Hu, L. Ma, D. Luo, J. Zheng, T. Wu, Y. Ren, J. Wen, F. Pan, K. Amine, *Nat. Energy*, 6 (2021) 277-286.
- [10] Q. Wang, S. Mariyappan, G. Rousse, A.V. Morozov, B. Porcheron, R. Dedryvère, J. Wu, W. Yang, L. Zhang, M. Chakir, M. Avdeev, M. Deschamps, Y.-S. Yu, J. Cabana, M.-L. Doublet, A.M. Abakumov, J.-M. Tarascon, *Nat. Mater.*, 20 (2021) 353-361.
- [11] M. Yoon, Y. Dong, J. Hwang, J. Sung, H. Cha, K. Ahn, Y. Huang, S.J. Kang, J. Li, J. Cho, *Nat. Energy*, 6 (2021) 362–371.
- [12] J. Chen, W. Deng, X. Gao, S. Yin, L. Yang, H. Liu, G. Zou, H. Hou, X. Ji, *ACS Nano*, 15 (2021) 6061–6104.
- [13] X. Yu, *Nat. Energy*, 6 (2021).
- [14] J. Chen, G. Zou, W. Deng, Z. Huang, X. Gao, C. Liu, S. Yin, H. Liu, X. Deng, Y. Tian, J. Li, C. Wang, D. Wang, H. Wu, L. Yang, H. Hou, X. Ji, *Adv. Funct. Mater.*, 30 (2020) 2004302.
- [15] J. Deng, X. Yu, X. Qin, D. Zhou, L. Zhang, H. Duan, F. Kang, B. Li, G. Wang, *Adv. Energy Mater.*, 9 (2019).
- [16] J. Masa, P. Weide, D. Peeters, I. Sinev, W. Xia, Z. Sun, C. Somsen, M. Muhler, W. Schuhmann, *Adv. Energy Mater.*, 6 (2016) 1502313.
- [17] R.A. House, U. Maitra, M.A. Pérez-Osorio, J.G. Lozano, L. Jin, J.W. Somerville, L.C. Duda, A. Nag, A. Walters, K. Zhou, M.R. Roberts, P.G. Bruce, *Nature*, 577 (2020) 502-508.
- [18] J. Huang, P. Zhong, Y. Ha, D.-H. Kwon, M.J. Crafton, Y. Tian, M. Balasubramanian, B.D. McCloskey, W. Yang, G. Ceder, *Nat. Energy*, 6 (2021) 706–714.
- [19] K. Zhang, Z. Jiang, F. Ning, B. Li, H. Shang, J. Song, Y. Zuo, T. Yang, G. Feng, X. Ai, D. Xia, *Adv. Energy Mater.*, 11 (2021) 2100892.
- [20] B. Li, H. Yan, J. Ma, P. Yu, D. Xia, W. Huang, W. Chu, Z. Wu, *Adv. Funct. Mater.*, 24 (2014) 5112-5118.
- [21] Y. Bi, J. Tao, Y. Wu, L. Li, Y. Xu, E. Hu, B. Wu, J. Hu, C. Wang, J.-G. Zhang, Y. Qi, J. Xiao, *Science*, 370 (2020) 1313-1317.
- [22] J. Zhao, X. Zhang, Y. Liang, Z. Han, S. Liu, W. Chu, H. Yu, *ACS Energy Lett.*, 6 (2021) 2552-2564.

- [23] S. Lee, W. Li, A. Dolocan, H. Celio, H. Park, J.H. Warner, A. Manthiram, *Adv. Energy Mater.*, 11 (2021) 2100858.
- [24] Y. Su, Q. Zhang, L. Chen, L. Bao, Y. Lu, S. Chen, F. Wu, *Journal of Energy Chemistry*, 65 (2022) 236-253.
- [25] C.-C. Su, M. He, J. Shi, R. Amine, Z. Yu, L. Cheng, J. Guo, K. Amine, *Energy Environ. Sci.*, 14 (2021) 3029-3034.
- [26] W. Liu, J. Li, W. Li, H. Xu, C. Zhang, X. Qiu, *Nat. Commun.*, 11 (2020) 1-11.

## TOC

The structure/interface coupling effect manipulated by the autocatalytic plating strategy is beneficial for mitigating the lattice oxygen loss and strengthening the crystal structure as well as electrode/electrolyte interface, rendering the highly reversible lithiation/delithiation process.

